

# FEM modelling of the three stages of friction stir spot welding

Gustavo E Carr<sup>1,2</sup>, Nicolás Biocca<sup>1,2</sup>, Guillermo A Lombera<sup>1,2</sup>  
and Santiago A Urquiza<sup>1</sup>

Proc IMechE Part C:  
J Mechanical Engineering Science  
1–10  
© IMechE 2023  
Article reuse guidelines:  
sagepub.com/journals-permissions  
DOI: 10.1177/09544062221148599  
journals.sagepub.com/home/pic  


## Abstract

A three-dimensional modelling of the Friction Stir Spot Welding process was carried out by means of a two-dimensional continuum with symmetry of revolution around the tool axis. The model included the plunging, dwelling and withdrawal stages of two 1.3 mm thick AA6061 alloy plates joining process. A highly viscous flow model was adopted, as well as the hypothesis of full stick contact between tool and material. The model was solved by means of the Finite Element Method (FEM) and Arbitrary Lagrangian Eulerian (ALE) techniques in an axisymmetric domain with mesh tracking and algorithms to account for contact and free flow. Numerical results were compared to experimental data found in literature. The maximum temperature for the pin front face was found within less than 5% of the experimental value. The velocity field were found close to those reported in literature and the final shape of the weld flash was similar to its experimental counterpart.

## Keywords

Friction stir spot welding, arbitrary Lagrangian Eulerian, finite element analysis, computational mesh dynamics, viscous flow, non linear behaviour

Date received: 2 August 2022; accepted: 9 December 2022

## Introduction

The Friction Stir Spot Welding process (FSSW) was introduced in 1991 by The Welding Institute, along with the Friction Stir Welding technique. These techniques are used to join materials without electric arc, fumes and radiation. Moreover, it can join dissimilar materials that can not be welded by arc.

Friction Stir Spot Welding is based on the action of a rotary tool pressed axially against the materials to be joined. The materials to be welded are usually two (sometimes three) overlapped plates. The tool consists of a cylinder called the shoulder, from which usually protrudes a smaller shape named the pin. Typically the shoulder's diameter ranges between 8 and 28 mm. The pin shape is mainly cylindrical or conical, but it can also be a triangular or square-based prism and even more complex shapes.

In FSSW three stages can be identified: *plunging*, *dwelling* and *withdrawal*. In the *plunging* stage, the tool spins at a constant speed and is pressed axially against the top plate, which leads to local temperature rise and plastic deformation takes place. Due to the temperature increase up to a 90% of the melting point, the material reaches a highly viscous plastic flow state. As the tool plunges into the plates, their materials are physically mixed. Once a prescribed

depth is reached, the tool is kept spinning but fixed in its vertical position. This stage is called *plunging*. Therefore, the *dwelling* stage follows, during which mixing continues and the heat generated by plastic work flows beyond the mixing zone. The last stage is the *withdrawal*, in which the tool is lifted and the welded plates cool down.

The rotational speed, the plunging speed and depth and the time span of the *dwelling* stage depend on the materials to join, their thicknesses, and tool dimensions.

Due to the existence of enormous spatial gradients of temperature and flow velocities that take place in very short distances, detailed experimental studies are challenging to carry out. For this reason, testing of FSSW involves robust machinery and complex setups.

<sup>1</sup>Computation-Aided Engineering Group (Grupo GIAC) Faculty of Mechanical Engineering - National University of Mar Del Plata, Mar Del Plata, Buenos Aires, Argentina

<sup>2</sup>CONICET, Argentina

## Corresponding author:

Gustavo E Carr, Computation-Aided Engineering Group (Grupo GIAC) Faculty of Mechanical Engineering - National University of Mar Del Plata, Av. Juan B. Justo 4302, Mar Del Plata, 7608BFQ, Argentina.  
Email: gecarr@fi.mdp.edu.ar

Therefore, numerical modelling becomes an excellent alternative tool for studying this welding process.

Success in numerical modelling is determined by adopting the correct constitutive equations and modelling techniques. There are systematic studies of the materials behaviour models, such as the one by Kuykendall<sup>1</sup> and D'Urso and Giardini.<sup>2</sup> There are also different approaches to FSSW depending on the representation of the materials behaviour, for it can be often described as an elastic-plastic solid or a highly viscous non-linear flow. Numerous works that use solid models can be cited, among them Mandal et al.<sup>3</sup> and Zhang et al.<sup>4</sup> On the other hand, viscous fluid models have the advantage of adequately describing high shear velocities processes, as of Jedrasiak and Shercliff.<sup>5</sup>

Among others, the remarkable motion of the computational domain is a significant challenge when modelling this joining process. In models that use Lagrangian description, extreme mesh deformations can occur and hinder their performance. Adaptive remeshing is often used to circumvent this inconvenience.<sup>6,7</sup> On the other hand, this technique can introduce artificial diffusion in the scalar and vector fields results. It also involves increasing computational time with the addition of mesh re-assembly processes. In the present work the Arbitrary Lagrangian-Eulerian (ALE) technique<sup>8,9</sup> has been used to avoid remeshing and artificial diffusion, for the expected gradients in the velocity field are steep. Also, given that the domain boundaries are movable in ways that depend on the results of the FSSW modelling, adopting ALE techniques is considered adequate to overcome the problems that arise with other techniques, as described previously.

In the literature, heat sources in thermal analysis were modelled differently according to the nature of the constitutive models adopted for the material. On the one hand, elastic-plastic models have the main advantage of computing residual stresses, as pointed out by Zhu et al.<sup>10</sup> These models were usually implemented with various heat sources due to contact friction type, such as Coulomb's,<sup>10</sup> Norton's,<sup>11</sup> combined<sup>12</sup> or other elaborate ad-hoc heat input functions.<sup>4,5,7</sup> A more detailed comparison between thermal analysis in FSW can be found in Meyghani et al.<sup>13</sup> On the other hand, non-linear viscous flow models such as the one adopted in the present work allow the implementation of a volumetric heat source, taking advantage of the nature of its governing equations. Miles et al.<sup>7</sup> used a similar axisymmetric approach as the present work but with a viscoplastic Norton-Hoff model and an updated Lagrangian scheme with explicit time integration on a commercial software. These authors used a modified dry Coulomb friction function to consider the saturation of contact stress. Using viscous fluid models also allows the use of full adhesion contact condition, also observed experimentally by Gerlich et al.<sup>14</sup> In the present work,

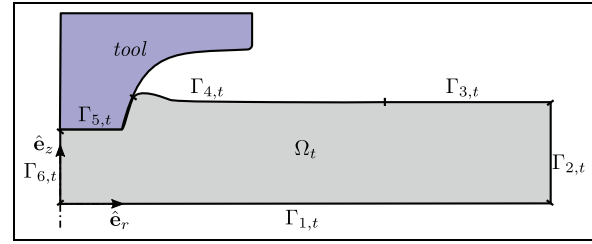


**Figure 1.** Problem setup. Nomenclature of the different elements of the domain and boundaries.

the numerical model was designed in order to compare its results with those of the aforementioned authors, given their very accurate temperature measurements obtained by placing thermocouples at 0.2 mm below the tool pin and shoulder surfaces. Also, the cited work provided a photograph of the actual tool, and its dimensions. These data were used to define the model parameters and tool geometries with a more precise representation.

The remainder of this document is organised as follows: Section *Methods* introduces the methods for the series of mechanical subproblems associated with the FSSW problem with adequate boundary conditions and initialisation. Also, the geometry tool description, material properties and the initial mesh discretisation employed, are provided. Section *Results* shows the computational results and the comparison with experimental data as found in Gerlich et al.<sup>14</sup> The discussion of these results is presented in Section *Discussion*. Final remarks are outlined in Section *Conclusions*.

## Methods

The whole FSSW process of two 1.3 mm alloy plates was modelled. The modelling time span was set from the initial tool contact at the beginning of the *plunging* stage until 2 s into the *withdrawal* stage.

Figure 1 shows the problem setup. Therein, the domain of interest  $\Omega_t$  (i.e. the alloy plates) and the spinning tool for an arbitrary configuration at the time  $t$  are shown, considering a plane axisymmetric geometry. On the same Figure the different boundaries can be seen, corresponding  $\Gamma_{1,t}$  to the material in contact with the backing plate,  $\Gamma_{2,t}$  to the continuation of the material,  $\Gamma_{3,t}$  to the upper fixed surface,  $\Gamma_{4,t}$  to the upper surface free of contact,  $\Gamma_{5,t}$  to the upper surface in contact with the tool and  $\Gamma_{6,t}$  to the axis of symmetry of the domain,  $\hat{e}_z$ .

The tool is made of H12 alloy steel and was represented in the model as an analytical solid, in the form of a sequence of segments defined by a set of  $(\hat{r}, \hat{z})$  coordinates. The tool pin minimum diameter was  $d_{min} = 3$  mm and the maximum diameter was  $d_{max} = 6$  mm, and its height was  $h_{pin} = 2$  mm. The tool shoulder diameter was  $D_{Shoulder} = 10$  mm. These

coordinates were calculated previously from the actual tool profile and were taken into account in the mesh movement sub-step. In the flow problem sub-step the flow velocities imposed at the contact interface were set by oblique conditions determined by the tool spinning and vertical displacement and by the mesh movement in the mesh dynamics problem sub-step. The vertical movement of the tool was a function of time. For the thermal sub-step, the material parameters and heat transfer coefficients were chosen for the corresponding alloy.

A full adherence contact condition between tool and material was adopted, after Gerlich et al.<sup>14</sup> These authors found that seizure wear conditions were found on the tool at 50 ms since the beginning of the welding process.

There are multiple sources of non-linearities that take place in this problem. Firstly, there is a contact condition between tool and material varying in time and space. This translates in the imposition of velocities in three dimensions and heat flow conditions that change with time. Furthermore, this leads to the movement of the material and hence the mesh, by means of flow tracking. This sets the problem in the context of moving deformable domains. Also, steep gradients of circumferential velocities develop. In addition, the velocity is dependant on both temperature and flow rate. The heat generation is a function of the deformation rate, and also both the heat conduction coefficient and heat capacity are functions of the local temperature.

All these characteristics that take place simultaneously were taken into account by means of a staggered solving approach. The problem solution was implemented by means of non-linearly iterating a sequence of three sub-steps for each time step. The resolution scheme is shown in subsection *Algorithm* and it is described in detail in subsection *Solving Sequence*. The mentioned sub-steps are described in the following subsections: *Flow Problem*, *Thermal Problem* and *Mesh Dynamics Problem*.

The choice for the volume domain mesh were LBB stabilised P1 elements. These elements have shown good numerical behaviour and low computational cost due to the low level of connectivity and low order Gauss quadrature required.<sup>15,16</sup>

### Solving the flow problem

The fluid problem was solved by means of the incompressible Navier-Stokes equations in Arbitrary Lagrangian-Eulerian (ALE) form. These equations were solved in a three-dimensional approach considering the directions  $\hat{\mathbf{e}}_r$ ,  $\hat{\mathbf{e}}_\theta$ ,  $\hat{\mathbf{e}}_z$  and axial symmetry around the  $\hat{z}$  axis. We assumed the following hypothesis for the velocity field:

$$\mathbf{v}(r, \theta, z) = v_r(r, z)\hat{\mathbf{e}}_r + v_\theta(r, z)\hat{\mathbf{e}}_\theta + v_z(r, z)\hat{\mathbf{e}}_z, \quad (1)$$

and for the pressure:

$$p = p(r, z). \quad (2)$$

The fluid problem reads as follows: find  $(\mathbf{v}, p) \in \Omega_t$  such that

$$\begin{cases} -\nabla p + 2 \operatorname{div}(\mu \boldsymbol{\epsilon}(\mathbf{v})) & = \rho \left( \frac{\partial \mathbf{v}}{\partial t} + \nabla \mathbf{v}(\mathbf{v} - \mathbf{v}_R) \right) \\ & \text{in } \Omega_t, \\ \operatorname{div} \mathbf{v} = 0 & \text{in } \Omega_t, \\ \mathbf{v}_R = \frac{\partial \mathbf{u}}{\partial t} & \text{in } \Omega_t, \\ \mathbf{P}(\hat{\mathbf{e}}_\theta) \mathbf{v} = \mathbf{0} & \text{on } \Gamma_{1,t}, \\ \mathbf{v} = \mathbf{0} & \text{on } \Gamma_{2,t} \cup \Gamma_{3,t}, \\ \boldsymbol{\sigma}(\mathbf{v}, p) \mathbf{n} = \mathbf{0} & \text{on } \Gamma_{4,t}, \\ \mathbf{P}(\hat{\mathbf{e}}_\theta) \mathbf{v} = \mathbf{f}(\mathbf{x}_t, t) & \text{on } \Gamma_{5,t}, \end{cases} \quad (3)$$

where  $\mathbf{v}_R$  denotes the fluid domain velocity, often called mesh velocity,  $\boldsymbol{\epsilon}(\mathbf{v})$  is the strain-rate tensor  $(\mathbf{v})^S = \operatorname{def} \frac{1}{2}(\mathbf{v} + \mathbf{v}^T)$ ,  $\mathbf{P}(\mathbf{n}) = \mathbf{I} - \mathbf{n} \otimes \mathbf{n}$  is the orthogonal projection operator over the plane with normal  $\mathbf{n}$ , and  $\boldsymbol{\sigma}_{(\mathbf{v}, p)} = -p\mathbf{I} + 2\mu\boldsymbol{\epsilon}(\mathbf{v})$  is the Cauchy stress tensor for a Newtonian flow. The function  $\mathbf{f}(\mathbf{x}_t, t)$  corresponds to the action of the tool on the material and is described in subsection *Mesh Dynamics Problem*. In addition, the material was considered as an incompressible fluid with density  $\rho$  and the dynamic viscosity

$$\mu = \frac{\sigma_e}{3\epsilon_e}, \quad (4)$$

where  $\epsilon_e$  is the second invariant of the effective deformation rate tensor

$$\epsilon_e = \sqrt{\frac{2}{3} \boldsymbol{\epsilon}(\mathbf{v}) \cdot \boldsymbol{\epsilon}(\mathbf{v})} \quad (5)$$

and  $\sigma_e$  is the equivalent plastic flow accordingly with the Sheppard and Wright model.<sup>17,18</sup>

$$\sigma_e = \frac{1}{\alpha} \ln \left[ \left( \frac{Z}{A} \right)^{1/n} + \left[ 1 + \left( \frac{Z}{A} \right)^{2/n} \right]^{1/2} \right] \quad (6)$$

where the Zener-Hollomon parameter  $Z$  is defined as

$$Z = \epsilon_e \exp \left( \frac{Q}{RT} \right). \quad (7)$$

The parameters  $\alpha$ ,  $A$ ,  $n$  and  $Q$  in equations (6) and (7) are material properties.

The governing differential equation (3) that describe the physical problem were set in their variational formulation form, more adequate to solve by the Finite Element Method. This led to a set of scalar equations which was solved using a general purpose solver framework developed by the authors' group since year 2001 and published elsewhere.<sup>19</sup>

The governing equation (3) have several sources of non-linearity, which were made evident explicitly by the convective term as well as implicitly through the referential domain description, the constitutive relation of the viscosity with the velocity (4) and temperature (7). The mentioned sources were linearised using

a fixed-point method detailed in subsection *Solving Sequence*.

For the temporal discretisation, an unconditionally stable and totally implicit *backward Euler* schema was used. Therefore, the resulting semi-discrete equations were discretised via FEM and stabilised by means of *Streamline Upwind/Petrov-Galerkin* (SUPG) introduced by Brooks and Hughes<sup>20</sup> and *Pressure Stabilising/Petrov-Galerkin* (PSPG) proposed by Tezduyar.<sup>21</sup>

### Solving the thermal problem

The thermal problem was solved by means of the energy equation in ALE form. As done with the fluid problem (see subsection *Flow Problem*), this equation was solved considering axial symmetry around the direction  $\hat{\mathbf{e}}_z$ . We assumed the following hypothesis for the temperature field:

$$T = T(r, z). \quad (8)$$

The thermal problem reads as follows: find  $T \in \Omega_t$  such that

$$\begin{cases} \rho C_p \left( \frac{\partial T}{\partial t} + \nabla T \cdot (\mathbf{v} - \mathbf{v}_R) \right) = \text{div}(k \nabla T) + \gamma & \text{in } \Omega_t, \\ q_n = h_{Steel} (T - T_{ref}) & \text{on } \Gamma_{1,t}, \\ q_n = h_{Al} (T - T_{ref}) & \text{on } \Gamma_{2,t}, \\ q_n = h_{Air} (T - T_{ref}) & \text{on } \Gamma_{3,t} \cup \Gamma_{4,t}, \\ q_n = h_{Tool} (T - T_{ref}) & \text{on } \Gamma_{5,t}, \end{cases} \quad (9)$$

where  $\gamma = \eta(\bar{\sigma} \cdot \epsilon)$  is a heat source per unit volume,  $\eta$  is the fraction of mechanical work transformed into heat,  $\bar{\sigma} = 2\mu\epsilon(\mathbf{v})$  is the deviatoric component of the Cauchy stress tensor and  $\epsilon(\mathbf{v})$  is the strain-rate tensor. Regarding the boundary conditions,  $q_n = -k \frac{\partial T}{\partial n}$  denotes a prescribed normal heat flux while  $h_{Steel}$ ,  $h_{Air}$ ,  $h_{Al}$  and  $h_{Tool}$  are the heat transfer coefficients for the the backing steel plate, aluminium, air and tool steel, respectively.<sup>22</sup>

In addition,  $T_{ref}$  is the reference temperature, usually  $T_{ref} = 20^\circ\text{C}$ .

The governing equation (9) have several sources of non-linearities. The heat capacity and the heat transfer coefficient are defined as  $C_p = C_p(T)$  and  $k = k(T)$ , respectively. On the other hand, the domain of resolution is  $\Omega_t = \Omega_t(\mathbf{u})$ , that is, depends on the displacement field  $\mathbf{u}$ , which also has sources of non-linearities (see subsection *Solving the Mesh Dynamics Problem*). Furthermore, the heat source per unit volume is  $\gamma = \gamma(\mathbf{v})$  whose dependency with the field  $\mathbf{v}$  is implicitly related with fields  $\mathbf{u}$  and  $T$ .

For the temporal discretisation, we used the second order accuracy Crank-Nicholson time integration scheme to satisfy the Geometric Conservation Law.<sup>23</sup> Therefore, the resulting semi-discrete equations were

discretised via FEM and stabilised by means of SUPG.

The constants for heat extraction calculation (whether conduction through the tool-material interface, boundary  $\Gamma_{5,t}$ , or by convection to open air, through boundaries  $\Gamma_{3,t}$  and  $\Gamma_{4,t}$ ) were determined by the contact condition for each time step. Heat extraction by conduction due to contact with the backup plates (boundary  $\Gamma_{1,t}$ ) was set as a Neumann condition, as was the extraction of heat by conduction through the plates, boundary  $\Gamma_{2,t}$ .

### Solving the mesh dynamics problem

The mesh dynamics problem, naturally arising from the ALE description of flow and thermal problems (see subsections *Flow Problem* and *Thermal Problem*, respectively), was solved via pseudo-elastic equations. These equations, considering the axial symmetry around the  $\hat{\mathbf{z}}$  axis, represent a two-dimensional problem in the current domain  $\Omega_t$ .

The mesh problem reads as follows: find  $(\mathbf{u}) \in \Omega_t$  such that

$$\begin{cases} (\lambda + G)\nabla(\text{div } \mathbf{u}) + G\nabla^2 \mathbf{u} = \mathbf{0} & \text{in } \Omega_t, \\ \mathbf{u} \cdot \hat{\mathbf{e}}_z = 0 & \text{on } \Gamma_{1,t}, \\ \mathbf{u} \cdot \hat{\mathbf{e}}_r = 0 & \text{on } \Gamma_{2,t}, \\ \mathbf{u} \cdot \hat{\mathbf{e}}_z = 0 & \text{on } \Gamma_{3,t}, \\ \mathbf{u} = (\mathbf{v} \cdot \mathbf{n})\mathbf{n} dt & \text{on } \Gamma_{4,t}, \\ \mathbf{u} = \mathbf{f}(\mathbf{x}_t, t) & \text{on } \Gamma_{5,t}, \\ \mathbf{u} \cdot \hat{\mathbf{e}}_r = 0 & \text{on } \Gamma_{6,t}, \end{cases} \quad (10)$$

being  $\lambda$  and  $G$  the Lamé's constants. In addition, these constants were stiffened through an element-based strategy based on element size and deformation modes regarding volume and shape changes by means of the well-known parameter  $\chi$ , introduced by Stein et al.<sup>24</sup> This parameter is a non-negative number that stiffens the elements proportionally to  $(J^e)^{-\chi}$ , being  $(J^e)$  the element Jacobian. When  $\chi = 0$  the method is reduced to a conventional elasticity problem. In the present work  $\chi = 1$  for the general dominion and  $\chi = 1.5$  in the zone associated to the tool contact interface.

With reference to boundary conditions, the displacement field over the boundaries  $\Gamma_{1,t}$ ,  $\Gamma_{2,t}$ ,  $\Gamma_{3,t}$  and  $\Gamma_{6,t}$  are prescribed to be null in the direction of the unit normal vector (i.e. the directions  $\hat{\mathbf{e}}_r$  and  $\hat{\mathbf{e}}_z$ ). On the other hand, the displacement field on the boundaries  $\Gamma_{4,t}$  and  $\Gamma_{5,t}$  correspond to the free surface motion and the tool-mesh contact dynamics, respectively. In the first case, the displacement field is set equal to the perpendicular velocity times the time step interval. In the case of the tool-mesh contact, without loss of generality the displacement field is determined by a two-dimensional vector-valued function related to the current coordinates and time, that is,  $\mathbf{f} = \mathbf{f}(\mathbf{x}_t, t) \forall \mathbf{x}_t \in \Gamma_{5,t}$ .

The tool-mesh contact and free surface movement was calculated using a special contact algorithm that involved upsampling the surface segments in boundaries  $\Gamma_{4,t}$  and  $\Gamma_{5,t}$  as a chain of ordered segments. The calculation of interference between the upsampled segment chain and the rigid solid tool geometry segments was carried out. The surface nodes that were not driven by the tool were free to move following the perpendicular projection of the material velocity nodal values. Downsampling was done to preserve the original proportional spacing between nodes along the contact boundary. Despite the success of this ad-hoc contact algorithm, and due to the nature of the process, excessive mesh distortion can not be prevented at the end of the *plunging* stage when more dense meshes are used and element collapse arises. The use of more sophisticated techniques such as of Takizawa et al.<sup>25,26</sup> and Biocca et al.<sup>27</sup> are recommended.

### Solving sequence

A staggered solving approach, shown in Algorithm 2.5 was used.

Three sub-steps were solved in sequence for each time step, and described as follows:

During the first sub-step the full Navier-Stokes equations were solved using ALE technique, as explained in section 2.1. In this sub-step the velocity and pressure fields were obtained, while mesh displacements, the associated mesh velocities and temperatures were held constant.

During the second sub-step heat balance differential equations were solved, taking into account the heat exchange across the domain boundaries, as described in section 2.2. All variables but temperature were held constant during this sub-step. The velocity field obtained in the previous sub-step were used to carry out the advection-diffusion differential equations solving by means of ALE technique.

During the third sub-step the mesh displacements in the  $(\hat{r}, \hat{z})$  plane were calculated by means of solving a linear elasticity problem (10) taking into account the radial and vertical velocities of the free surface nodes and the nodes under the tool action, as stated in section 2.3. All remaining variables (i.e.  $\mathbf{v}$  and  $p$  fields) were held constant during this sub-step.

For each variable a comparison was carried out between the previous iteration values and those of the current one. Once these differences fell under their respective tolerances it was assumed that convergence of the solution had been achieved, therefore a new time step calculation cycle would begin.

### Algorithm

Loop in time for step  $n + 1$ .

$$\mathbf{u}^k = \mathbf{u}_n$$

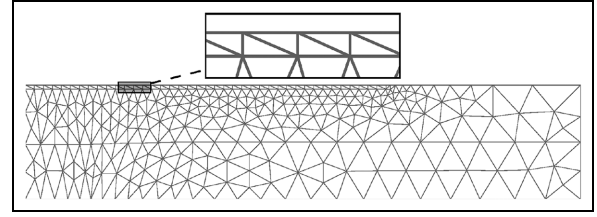


**Figure 2.** Two-dimensional initial mesh used for the resolution of FSSW joining. In the close-up view, the thin layer mesh is shown.

Evaluate:  $\mu = \frac{\sigma_e}{3\epsilon_e}$ , using  $\epsilon_e = \epsilon_e(\mathbf{v}^k)$  and  $\sigma_e = \sigma_e(Z(T^k))$ ;  $\sigma_e = \sigma_e(Z(T^k))$ ; (see equations (6) and (7), respectively)

Non linear loop for FSSW coupled problem, iteration  $k + 1$ .

Solve iteratively linearised flow problem, equation (3)  $\rightarrow \mathbf{u}^{k+1}$

- Evaluate:  $\mathbf{v}_R^{k+1} = \frac{\mathbf{u}^{k+1} - \mathbf{u}_n}{dt}$  in  $\Omega_t(\mathbf{u}^{k+1})$

Solve thermal problem, equation (9)  $\rightarrow T^{k+1}$

Solve mesh dynamics problem, equation (10)

- Evaluate:  $\mathbf{u}^{k+1} = (\mathbf{v}^{k+1} \cdot \mathbf{n}^{k+1}) \mathbf{n}^{k+1} dt$

on  $\Gamma_{4,t}(\mathbf{u}^k)$

Evaluate convergence using the fields  $\mathbf{v}^{k+1}$ ,  $\mathbf{u}^{k+1}$  and  $T^{k+1}$

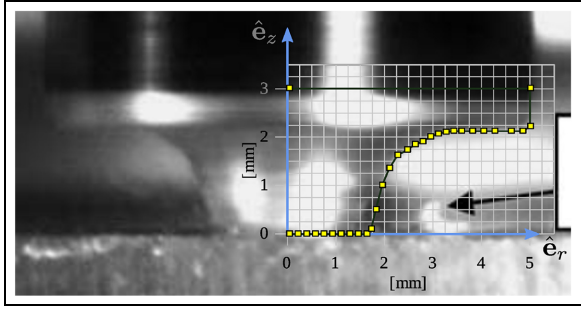
### Initial mesh discretisation

Figure 2 shows the mesh discretisation for the two-dimensional domain of interest. The amount of elements and nodes were 649 and 1211, respectively. The initial aspect ratio of the elements was conveniently designed in order to reduce high distortions during the introduction stage. Therein, three mesh regions can be observed: lower sheet and upper sheet with contact sub zone (see close-up view in Figure 2).

### Tool geometry and physical model parameters

The tool profile was defined by a series of segments joining counter clockwise consecutive points in plane  $rz$  (i.e. radii and heights), in the shape of a closed polygon with symmetry around  $\hat{z}$  axis. In order to feed our model with a more precise representation, it was defined based on its dimensions and the actual image of it as seen in Gerlich et al.<sup>14</sup> Both tool profile definition and source picture are shown in Figure 3

It is worth noting that the cited authors used thermocouples placed 0.2 mm below the surface of the pin and the shoulder front faces, therefore the temperature measurements were quite close to those of the material.



**Figure 3.** Tool geometry for the present work model. The background image of the actual tool was taken from Gerlich et al.<sup>14</sup> The tool profile is shown in black with yellow dots.

**Table 1.** Chemical composition for AA6061 alloy.<sup>28</sup>

Element	%
Al	Base
Si	0.4 - 0.8
Fe	≤ 0.7
Cu	0.04 - 0.35
Mn	0.15
Mg	1.2
Cr	0.04 - 0.35
Zn	≤ 0.25
Ti	≤ 0.15

The alloy chosen for the model was AA6061, and its composition is shown in Table 1.

The process parameters were set as follows: total material thickness  $e = 2.6$  mm, tool rotational speed  $\Omega = 1000$  rpm, shoulder diameter  $\Phi_h = 10$  mm, pin diameter  $\Phi_p = 4$  mm, pin length  $h = 2$  mm, plunging speed  $v_z = 0.75$  mm/s, dwelling time  $t_d = 4$  s and tool plunging depth  $h_f = 2.2$  mm.

The heat capacity and heat transfer coefficient were defined with the following polynomials<sup>29</sup>:

$$C_p(T) = 929 - 6.27 \cdot 10^{-1} T + 1.48 \cdot 10^{-3} T^2 - 4.33 \cdot 10^{-8} T^3 \left[ \frac{\text{J}}{\text{kgK}} \right], \quad (11)$$

$$k(T) = 25.2 + 3.98 \cdot 10^{-1} T + 7.36 \cdot 10^{-6} T^2 - 2.52 \cdot 10^{-7} T^3 \left[ \frac{\text{W}}{\text{mK}} \right]. \quad (12)$$

The material constants for AA6061 alloy according to the Sheppard and Wright model were:  $\ln A = 26.707$ ,  $\alpha = 0.01$  [1/MPa],  $n = 9.16$  and  $Q = 143890$  [J/mol].

The value for the fraction of mechanical work transformed into heat was  $\eta = 0.9$  as per Ulysse.<sup>30</sup>

The heat transfer coefficient between the material and the backing plate was:  $h_{Steel} = 11$   $\left[ \frac{\text{W}}{\text{m}^2\text{K}} \right]$  (boundary  $\Gamma_{1,t}$ ),<sup>22</sup> while the heat transfer coefficient through boundary  $\Gamma_{2,t}$  was  $h_{Al} = 1000$   $\left[ \frac{\text{W}}{\text{m}^2\text{K}} \right]$  representing the

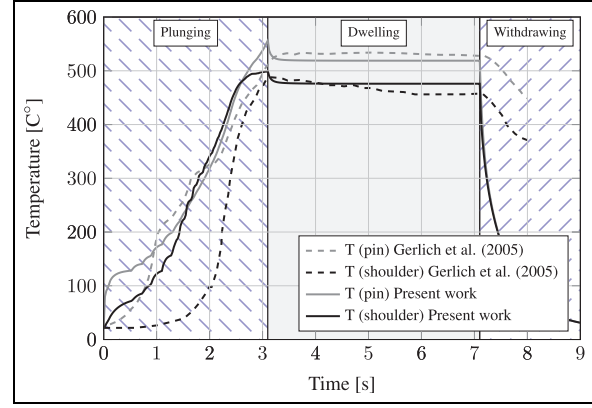


**Figure 4.** Experimental results for pin and shoulder temperatures as of Gerlich et al.<sup>14</sup> Numerical results of temperature values at corresponding points in the domain.

continuation of the material. The heat transfer coefficient to open air ( $\Gamma_{3,t}$  and  $\Gamma_{4,t}$ ) was  $h_{Air} = 5$   $\left[ \frac{\text{W}}{\text{m}^2\text{K}} \right]$ . The heat transfer coefficient between the material and the tool ( $\Gamma_{5,t}$ ) was:  $h_{Tool} = 300$   $\left[ \frac{\text{W}}{\text{m}^2\text{K}} \right]$ .

The tool thermal parameters were as follows: the heat capacity  $C_p = 5.6$   $\left[ \frac{\text{N}}{\text{mm}^2\text{K}} \right]$  and the conductivity  $k = 28.4$   $\left[ \frac{\text{W}}{\text{mK}} \right]$ .

## Results

On Figure 4 experimental results as of Gerlich et al.<sup>14</sup> are shown along with numerical results of temperature values at their corresponding points in the domain.

On Figure 5 the circumferential velocity field at four *plunging* stage time frames are shown:  $t = 0, 0.5, 1.0$  and  $1.5$  s.

On Figure 6 circumferential velocity field is shown for six time frames of the *plunging* stage:  $t = 2.0, 2.25, 2.5, 2.75, 3.0$  and  $3.25$  s. After  $t = 3.1$  s the *dwelling* stage begins, during which there is negligible variation in the circumferential velocity field and the vertical and radial velocities are null. After  $t = 7.1$  s the *withdrawing* stage begins. The velocity field is null throughout the domain and the material cools down until reaching ambient temperature. On Figure 7 the vertical ( $\hat{z}$  axis) and radial ( $\hat{r}$  axis) velocities are shown in the form of vectors for four-time frames during the *plunging* stage.

## Discussion

There is no perfect model for representing the joining process throughout, given that the material at the laboratory is actually behaving like a viscous fluid at the stirred zone (at  $T \approx 0.9T_{melt}$ ) and as a solid at the heat affected zone and beyond, with a smooth transition in between. Constitutive models, such as Johnson-Cook, are well suited for solving the solid material behaviour, while others such as Sheppard-

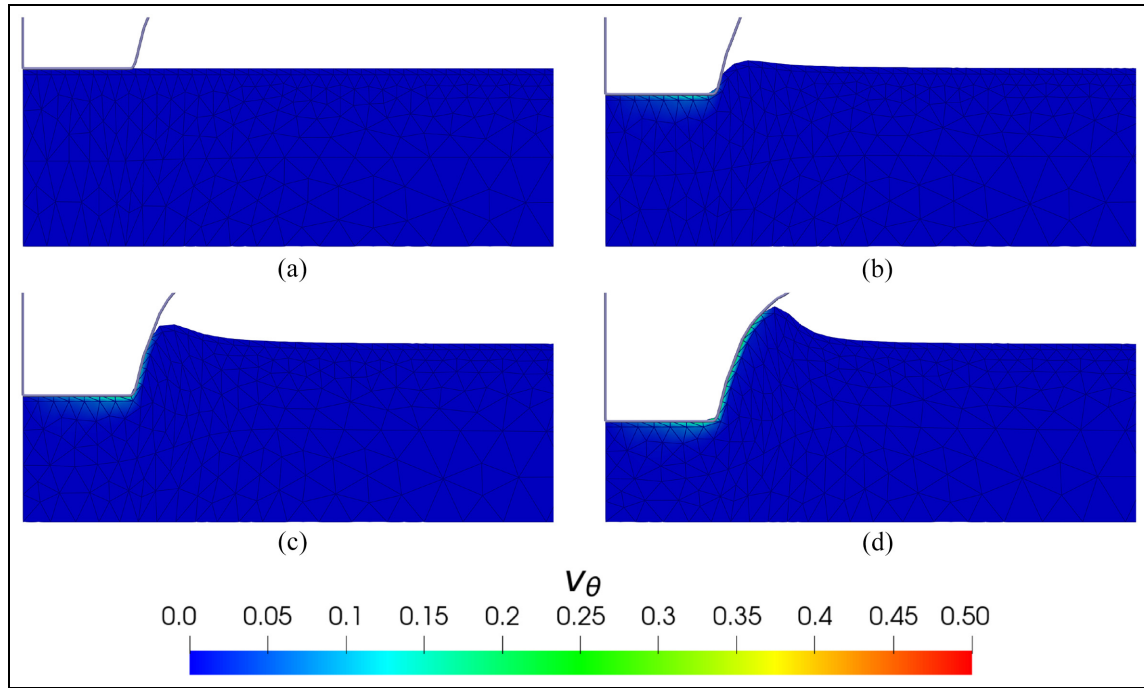


**Figure 5.** Plunging stage. Circumferential velocity field for range  $0 \leq t \leq 1.5$  s: (a)  $t = 0$  s, (b)  $t = 0.5$  s, (c)  $t = 1.0$  s and (d)  $t = 1.5$  s.

Wright as used in this work are better suited for high strain rates like in a viscous flow.

The dynamic viscosity function  $\mu$  used for the numerical computation of the FSSW process (Equation (4)) is inversely proportional to the temperature through the Zenner-Hollomon parameter (Equation (7)) present in the flow stress equation (Equation (6)). In turn, temperature is proportional to the heat source, given by the flow stress inner product with the strain rate tensor. Since the beginning of the joining process (Figure 5(a)), the high strain rate zone developed in the material near the contact interface becomes the source of heat which is conducted and convected to the surroundings. This local temperature increment provokes a drop in the local viscosity and a high temperature gradient which in turn, lowers the dynamic viscosity gradient until an equilibrium is reached, at each time step.

Figure 4 shows the temperature values of nodes in contact with the tool at the same radius as the experimental thermocouples were located. It can be seen that for  $t \leq 1$  s, the numerical model values of the pin have a larger increase than those of the real tool since the thermocouple is embedded in the tool steel, while the numerical result corresponds to the material undergoing high shear rates. Notice that at the beginning of the considered time span (i.e.  $t \leq 1$ ), the shoulder temperature results show a steeper curve than the experimental measurements. This outcome may be due to the fact that the shoulder starts to make contact with the material when  $t > 2.1$  s. The thermocouple embedded in the tool shoulder measured the temperature of the steel tool, while for  $t < 2.1$  s the corresponding nodes in the model were

heated by conduction through the aluminium alloy, which has a higher coefficient of heat conduction than that of the steel. Since  $t \approx 2.1$  s, the flat surface of the shoulder made contact with the material and hence, the temperature values for the corresponding node in the continuum were closer to those obtained experimentally.

There is a slight drop in temperature between the last part of the *plunging* stage before the *dwelling* stage ( $2.5 \text{ s} < t < 3.1 \text{ s}$ ). This may be because at time  $t = 2$  s (Figure 6(a)) the tool shoulder starts to squeeze material outwards from the tool axis and therefore the strain rate near the interface is higher than before, leading to an increase in viscous forces dissipated as heat. At the *dwelling* stage only the circumferential velocity field is present and hence, heat input is a little lower than previously.

During the *withdrawal* stage, the temperature curves diverge for the simple reason that the thermocouples read the tool temperature as it cooled down while the nodes show the welded material temperature evolution.

The early tool seizure condition in experimental FSSW (found at  $t = 50$  ms since the tool contact) as reported by Gerlich et al.<sup>14</sup> showed that such a condition could be adopted for the present model aiming to reproduce the physical phenomenon as close as possible. This choice implied some new issue that had to be addressed. Due to contact, the velocity at the tool-workpiece boundary had to be imposed as oblique conditions, spawning additional velocity coupling terms in the global system of equations. Also, these velocities at the boundary had to be gradually imposed, as in Ulysse<sup>30</sup> to minimise instability and

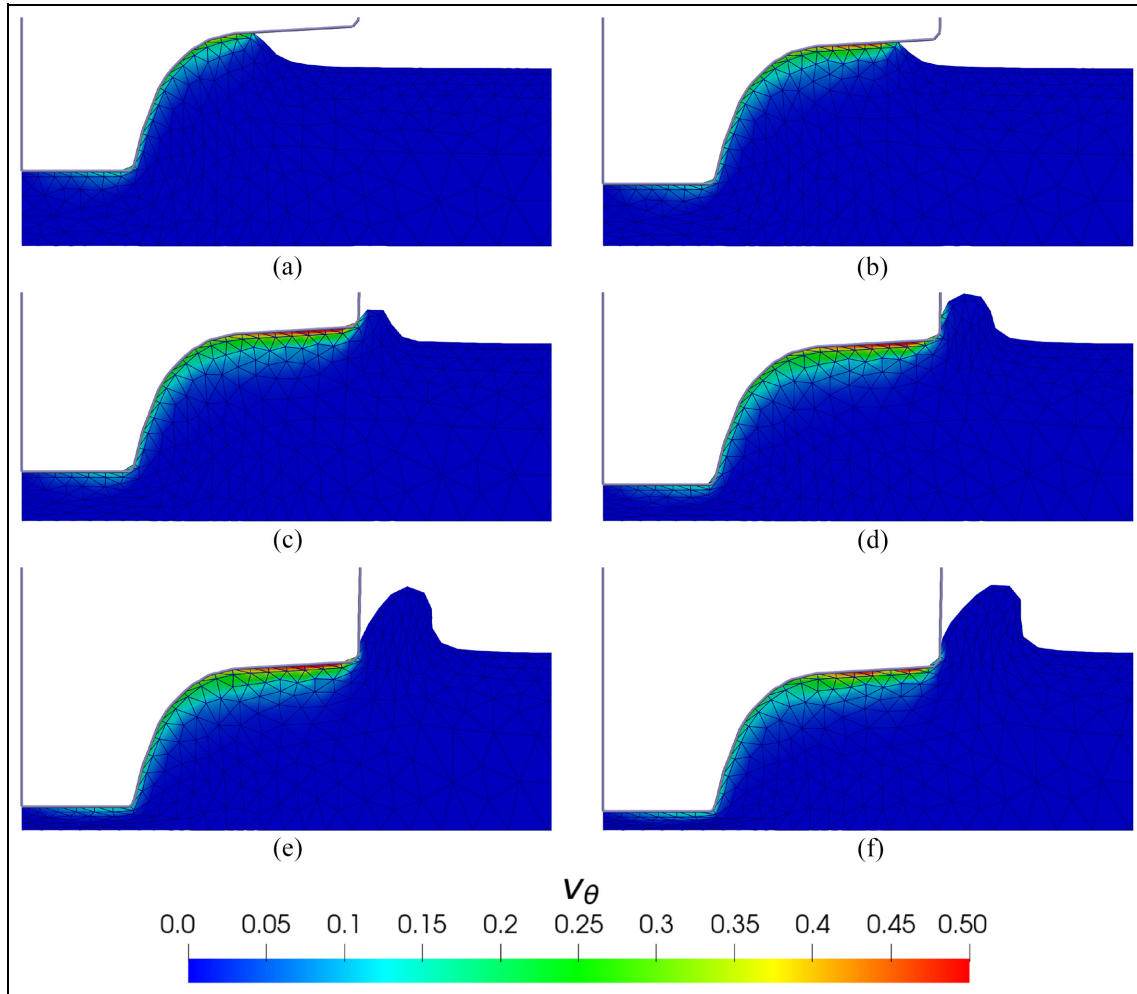


**Figure 6.** Plunging stage. Circumferential velocity field for range  $2.0 \leq t \leq 3.25$  s: (a)  $t = 2.00$  s, (b)  $t = 2.25$  s, (c)  $t = 2.50$  s, (d)  $t = 2.75$  s, (e)  $t = 3.00$  s and (f)  $t = 3.25$  s.

convergence issues. The introduction of an auxiliary contact variable was also needed, since it played an important role in the smooth transition from free surface nodes to penalised nodes (in terms of velocities).

We observed that the temperature curves fit well to the experimental values, mainly in the *dwelling* stage. Therefore, it can be considered that both the condition of adherence throughout the contact surface and the heat loss coefficients and boundary conditions were well chosen.

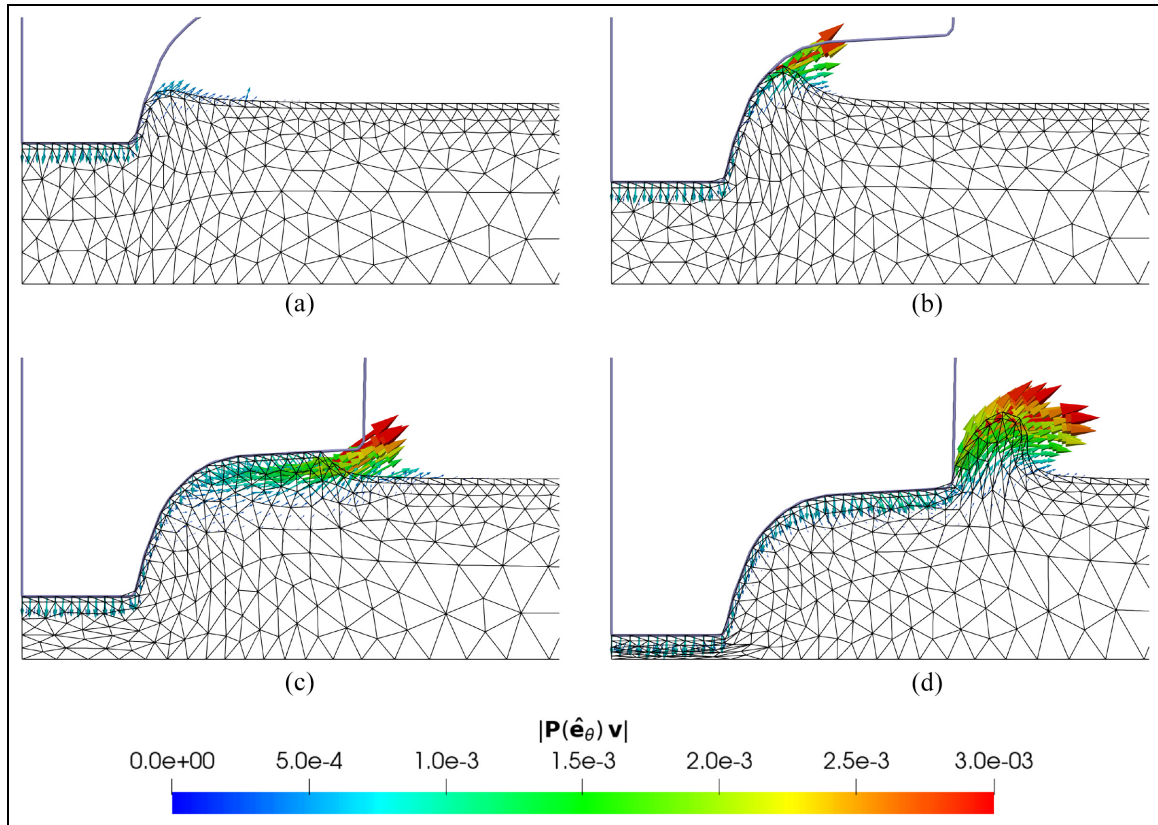
From Figures 5 and 6, it can be observed that the highest circumferential velocities were found in the zone next to the tool surface, as well as the highest gradients of  $V_\theta$  in the vertical direction,  $\hat{e}_z$ . A particular condition that may have led to an oscillatory behaviour was found at that location. The high velocity gradients led to an increase in the amount of local plastic work and thus in the temperature. This, in turn, decreased the local values of viscosity  $\mu$ , which lowered the effective stress  $S_{Eff}$ . This phenomenon was one of the main issues to deal with while achieving the solution.

Figure 7 shows the flow velocities in radial  $\hat{e}_r$  and vertical  $\hat{e}_z$  directions. It can be seen that a flow of

material was developed in a zone very close to the tool surface. This flow had a maximum value at a small distance below the contact surface. This may be due to the cooling effect that the tool exerted on the material, added to the adherence contact condition adopted. These results, in turn, were coincident with those of Hirasawa et al.<sup>31</sup> who used the Particle Method<sup>32</sup> with a similar tool geometry to the one used in this work.

It can also be seen that the tool plunged into the material at a constant rate, while the flow velocity at the free surface increased until a crown of debris was generated. The shape of the displaced material is characteristic of this type of welding process whenever there is some degree of shoulder plunging, as seen in Zhang et al.<sup>4</sup> and Reilly et al.,<sup>33</sup> to name a few.

Regarding the issues about solving the model for the whole process, it turned out to be better to consider the viscosity as a variable field within each element (i.e. compute the viscosity at each Gauss point) instead of constant across elements. This approach led to better conditioned sub-steps coupling achieving faster convergence for the solution. The viscosity calculus as a temperature function turned out to be



**Figure 7.** Plunging stage sequence. Velocity field in [m/s] for directions  $\hat{e}_r$  and  $\hat{e}_z$  for the time range  $0.75 \leq t \leq 3.0$  s: (a)  $t = 0.75$  s, (b)  $t = 1.50$  s, (c)  $t = 2.25$  s and (d)  $t = 3.00$  s.

crucial. Otherwise, the maximum values of the latter would have resulted far from the experimental data.

## Conclusions

Numerical modelling of the whole Friction Stir Spot Welding process was carried out using the Finite Element Method on a two-dimensional domain with symmetry of revolution. Accordingly, a computational tool for modelling the whole process was developed.

The model comprises three sub-steps for each time step: a first one solving the Navier-Stokes equations for an incompressible non-linear fluid using Arbitrary Lagrangian-Eulerian (ALE) techniques, a second sub-step solving the heat balance equations using ALE techniques and integrating on as time-dependent domain using a Crank-Nicholson schema, and finally, a third sub-step calculating the mesh shape evolution in the two-dimensional domain through the resolution of pseudo-elasticity equations. The time discretisation for the first two sub-steps was made using a Crank-Nicholson strategy.

The modelling thermal outcomes were compared to those of literature. The obtained curves showed a very good adjustment to experimental data, within 5% of its maximum values. These results may lead us to consider that full sticking hypothesis, heat generation and heat transfer conditions were well chosen. In

addition, the final weld flash geometry was found similar quite close to those that of experimental counterparts with same proportion of shoulder plunging. Besides, the velocity field was qualitatively close to those found in literature.

Despite the good agreement in temperature values after considering tool-workpiece full adherence, further work needs to be carried out on the contact conditions model in order to take into account the possibility of dry friction between the tool and the material, given that this phenomenon was observed experimentally very shortly at the beginning of the welding process.

## Declaration of conflicting interests

The author(s) declared no potential conflicts of interest with respect to the research, authorship, and/or publication of this article.

## Funding

The author(s) disclosed receipt of the following financial support for the research, authorship, and/or publication of this article: Consejo Nacional de Investigaciones Científicas y Técnicas (CONICET) and grants “Simulación Computacional de Sistemas Mecánicos No-Lineales” (15/G497) and National University of Mar del Plata (UNMDP), Argentina, through grants: “Modelización Computacional de Problemas Multifísica”.

## References

1. Kuykendall KL. An evaluation of constitutive laws and their ability to predict flow stress over large variations in temperature, strain, and strain rate characteristic of friction stir welding. <https://scholarsarchive.byu.edu/etd/2768> (2011, accessed March 2018).
2. D'Urso G and Giardini C. Fem model for the thermo-mechanical characterization of friction stir spot welded joints. *Int J Mater Forming* 2016; 9(2): 149–160.
3. Mandal S, Rice J and Elmustafa AA. Experimental and numerical investigation of the plunge stage in friction stir welding. *J Mater Process Technol* 2008; 203(1–3): 411–419.
4. Zhang B, Chen X, Pan K, et al. Thermo-mechanical simulation using microstructure-based modeling of friction stir spot welded AA 6061-T6. *J Manuf Process* 2019; 37: 71–81.
5. Jedrasiak P and Shercliff HR. Small strain finite element modelling of friction stir spot welding of al and mg alloys. *J Mater Process Technol* 2019; 263: 207–222.
6. Guerdoux S. Numerical simulation of the friction stir welding process using both Lagrangian and arbitrary Lagrangian Eulerian formulations. *AIP Conf Proc* 2004; 712: 1259.
7. Miles M, Karki U and Hovanski Y. Temperature and material flow prediction in friction-stir spot welding of advanced high-strength steel. *JOM* 2014; 66(10): 2130–2136.
8. Donea J, Huerta A, Ponthot JP, et al. Arbitrary Lagrangian-Eulerian methods. In: Stein E, Thomas J.R. Hughes, (eds) *The encyclopedia of computational mechanics*. Hoboken: John Wiley & Sons, Ltd, 2004, pp.413–437, Vol. 1. DOI:10.1002/9781119176817.ecm2009.
9. Hughes TJR, Liu WK and Zimmermann TK. Lagrangian-eulerian finite element formulation for incompressible viscous flows. *Comput Methods Appl Mech Eng* 1981; 29(3): 329–349. <https://www.sciencedirect.com/science/article/pii/0045782581900499>. Accessed March, 2018.
10. Zhu Z, Wang M, Zhang H, et al. A finite element model to simulate defect formation during friction stir welding. *Metals* 2017; 7(7): 256.
11. Fourment L and Guerdoux S. 3d numerical simulation of the three stages of friction stir welding based on friction parameters calibration. *Int J Mater Forming* 2008; 1(S1): 1287–1290.
12. Khosa SU, Weinberger T and Enzinger N. Thermo-mechanical investigations during friction stir spot welding (FSSW) of AA6082-T6. *Weld World* 2010; 54(5–6): R134–R146.
13. Meyghani B, Awang M, Emamian SS, et al. A comparison of different finite element methods in the thermal analysis of friction stir welding (FSW). *Metals* 2017; 7(10): 450.
14. Gerlich A, Su P and North TH. Tool penetration during friction stir spot welding of al and mg alloys. *J Mater Sci* 2005; 40(24): 6473–6481.
15. Karabelas E, Haase G, Plank G, et al. Versatile stabilized finite element formulations for nearly and fully incompressible solid mechanics. *Comput Mech* 2020; 65(1): 193–215.
16. Pironneau O. On the transport-diffusion algorithm and its applications to the Navier-Stokes equations. *Numer Math* 1982; 38: 309–332.
17. Li Z, Yue Y, Ji S, et al. Optimal design of thread geometry and its performance in friction stir spot welding. *Mater Des* 2016; 94: 368–376. <https://www.sciencedirect.com/science/article/pii/S026412751630082X>. Accessed March 2018.
18. Sun Z, Wu CS and Kumar S. Determination of heat generation by correlating the interfacial friction stress with temperature in friction stir welding. *J Manuf Process* 2018; 31: 801–811.
19. Urquiza S and Venere M. An application framework architecture for fem and other related solvers. *Mec Comput* 2001; XXI: 3099–3109.
20. Brooks AN and Hughes TJR. Streamline upwind/Petrov-Galerkin formulations for convection dominated flows with particular emphasis on the incompressible Navier-Stokes equations. *Comput Methods Appl Mech Eng* 1982; 32(1–3): 199–259.
21. Tezduyar T. Stabilized finite element formulations for incompressible flow computations. *Adv Appl Mech* 1991; 28: 1–44.
22. Kang J, Lee K and Kang S. Heat transfer coefficient for F.E. Analysis in the warm forging process. *J Achiev Mater Manuf Eng* 2006; 20(1–2): 367–370.
23. Farhat C, Geuzaine P and Grandmont C. The discrete geometric conservation law and the nonlinear stability of ALE schemes for the solution of flow problems on moving grids. *J Comput Phys* 2001; 174(2): 669–694.
24. Stein K, Tezduyar T and Benney R. Mesh moving techniques for fluid-structure interactions with large displacements. *J Appl Mech* 2003; 70(1): 58–63.
25. Takizawa K, Tezduyar TE and Avsar R. A low-distortion mesh moving method based on fiber-reinforced hyperelasticity and optimized zero-stress state. *Comput Mech* 2020; 65: 1567–1591.
26. Takizawa K, Tezduyar TE, Boben J, et al. Fluid-structure interaction modeling of clusters of spacecraft parachutes with modified geometric porosity. *Comput Mech* 2013; 52(6): 1351–1364.
27. Biocca N, Blanco PJ, Caballero D, et al. A biologically-inspired mesh optimizer based on pseudo-material remodeling. *Comput Mech* 2022; 69: 505–525.
28. Yang S. *Comportement et endommagement des alliages d'aluminium 6061-T6: approche micromécanique*. PhD Thesis, Ecole Nationale Supérieure des Mines de Paris, 2012.
29. Arora A, De A and DebRoy T. Toward optimum friction stir welding tool shoulder diameter. *Scr Mater* 2011; 64(1): 9–12.
30. Ulysse P. Three-dimensional modeling of the friction stir-welding process. *Int J Mach Tools Manuf* 2002; 42(14): 1549–1557. <https://www.sciencedirect.com/science/article/pii/S0890695502001141>. Accessed March 2018.
31. Hirasawa S, Badarinarayan H, Okamoto K, et al. Analysis of effect of tool geometry on plastic flow during friction stir spot welding using particle method. *J Mater Process Technol* 2010; 210: 1455–1463.
32. Hirasawa S. Combined analysis of plastic deformation flow and temperature distribution during friction stir welding. In: *Proceedings of the ASME 2005 international mechanical engineering congress and exposition, 2005*. ASME.
33. Reilly A, Shercliff H, Chen Y, et al. Modelling and visualisation of material flow in friction stir spot welding. *J Mater Process Technol* 2015; 225: 473–484.